Nano Research

Open Access

Research Article

HULU: A unified Monte Carlo framework for adsorption simulations with machine learning potentials

Xitai Cai[1], Yuxun Wu[1], Libo Li[1] ✉, Lijun Liao[1], Penghua Ying[2,3] ✉, and Yanying Wei[1] ✉

[1] *School of Chemistry and Chemical Engineering, Guangdong Provincial Key Lab of Green Chemical Product Technology, State Key Laboratory of Advanced Papermaking and Paper-based Materials, South China University of Technology, Guangzhou 510640, China*
[2] *Laboratory for multiscale mechanics and medical science, SV LAB, School of Aerospace, Xi'an Jiaotong University, Xi'an 710049, China*
[3] *Department of Physical Chemistry, School of Chemistry, Tel Aviv University, Tel Aviv 6997801, Israel*

Cite this article: *Nano Research*, **2026**, *19*, 94908548. https://doi.org/10.26599/NR.2026.94908548

ABSTRACT: Adsorption in nanoporous materials is pivotal for addressing global challenges in gas storage, separation, sensing, catalysis, and atmospheric water harvesting. Consequently, molecular simulations are essential for understanding adsorption mechanisms and accelerating material discovery. Key thermodynamic descriptors, such as adsorption isotherms, density distributions, and Henry constants, are particularly valuable for high-throughput screening and predicting separation performance. Recently, machine learning potentials (MLPs) have emerged as a powerful tool, offering near-*ab-initio* accuracy with high computational efficiency. While MLPs have been extensively applied in molecular dynamics simulations, their integration into Monte Carlo (MC) simulations for adsorption remains largely untapped. This limitation arises primarily because mainstream MC simulation codes are designed for empirical force fields and lacks native support for MLPs. In this work, we developed a flexible Python package, high-throughput vniversal learning-enabled utility for adsorption (HULU), to bridge this gap. We present the first demonstration of calculating full adsorption isotherms using state-of-the-art foundation MLPs (MACE-MATPES-PBE-0, NEP89, and ORB v3). Furthermore, we systematically benchmark these models against standard baselines, such as available experimental or density-functional-theory calculation data, and elucidate the microscopic origins of deviations in the simulation results. Ultimately, HULU paves the way for incorporating high-fidelity MLPs into high-throughput screening workflows, significantly enhancing the predictive design of nanoporous materials for energy and environmental applications.

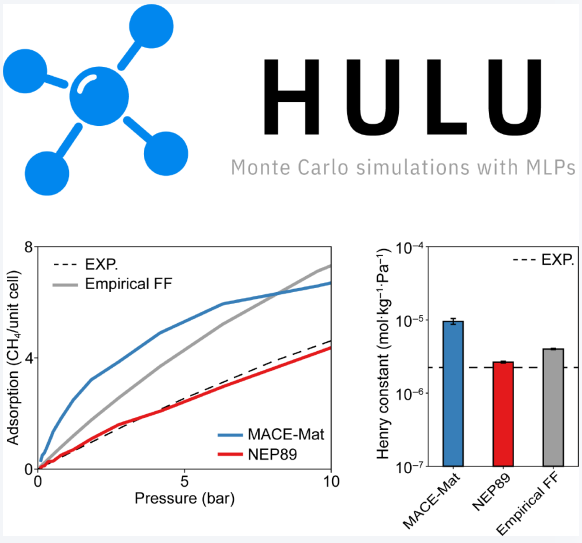

KEYWORDS: adsorption simulation, grand canonical Monte Carlo, Widom insertion, machine learning potentials, nanoporous materials

1 Introduction

Adsorption in nanoporous materials plays a crucial role in a wide range of applications, including gas storage [1–3], separation [4–7], catalysis [8, 9], and atmospheric water harvesting [10–12]. Consequently, accurate adsorption simulations are essential for advancing and optimizing these applications [13, 14]. For example, adsorption isotherms obtained from grand canonical Monte Carlo (GCMC) simulations are widely used to predict separation performance [15–17]. In addition, density distributions sampled from canonical Monte Carlo (CMC) simulations provide microscopic insights into preferential adsorption sites [18, 19]. Moreover, thermodynamic descriptors such as Henry constants and heats of adsorption, calculated using the Widom insertion method, enable the rapid high-throughput screening of thousands of candidate nanoporous materials [20–22].

Received: January 5, 2026; **Revised:** February 6, 2026
Accepted: February 6, 2026

✉Address correspondence to Libo Li, celbli@scut.edu.cn; Penghua Ying, penghua@xjtu.edu.cn; Yanying Wei, ceyywei@scut.edu.cn

Recently, machine learning potentials (MLPs) have undergone rapid development, demonstrating near-*ab-initio* accuracy in molecular simulations [23–25]. Several representative MLP frameworks, such as ACE [26–28], DP [29–31], MACE [32, 33], NEP [34–36], NequIP [37], and ORB [38, 39], have been developed in recent years and have been extensively applied in molecular dynamics (MD) simulations [40, 41]. In contrast, their application in MC simulations remains largely untapped. This gap between MD and MC simulations largely stems from the fact that most widely used MC simulation codes, such as RASPA2 [42], Cassandra [43], and Music [44], were developed for empirical force fields (FFs) and lack native support for MLPs, limiting their adoption in adsorption simulations. Although very recently MC simulations have begun to be explored using MLPs [45], MLP-based GCMC simulations, e.g., capable of producing full adsorption isotherms and other critical adsorption properties, have not yet been reported. Also, a systematic investigation and benchmarking of adsorption in nanoporous materials remains absent.

In this work, we develop high-throughput universal learning-enabled utility for adsorption (HULU), a flexible Python package specifically designed to bridge this gap by enabling MC simulations across diverse MLPs to determine adsorption properties. Unlike previous general frameworks, HULU is specifically designed for adsorption workflows, offering integrated post-analysis functions for the automated calculation of isotherms, Henry constants, and density distributions. Comprehensive validations were performed against MD simulations and widely used simulation codes to assess its accuracy of MC sampling. Using HULU, we present the first full adsorption isotherms for CH_4 in ZIF-8 with MLPs, along with a systematic investigation that benchmarks three representative foundation MLP models—MACE-MATPES-PBE-0 (hereafter referred to as MACE-Mat), NEP89, and ORB v3—against traditional simulation results. Furthermore, we analyzed how discrepancies in the interactions predicted by three MLPs influence MC statistics, thereby providing an in-depth assessment of MLP reliability for predicting gas–solid interactions in nanoporous materials.

2 Computational details

2.1 Monte Carlo simulations

MC simulations were performed using HULU, the modular Monte Carlo framework developed in this work, also with the open-source code RASPA2 [42] for comparison. All simulations were conducted at a temperature of 313.15 K under periodic boundary conditions. MC simulations were used to compute adsorption-related thermodynamic and structural properties, including adsorption isotherms, Henry constants, heats of adsorption, and equilibrium density distributions.

For RASPA2 simulations, a typical MC run consisted of 1×10^5 equilibration cycles followed by 1×10^5 production cycles. For HULU, we employed 5×10^5 steps for equilibration and an additional 5×10^5 steps for production. For HULU, these MC steps were verified to achieve statistical convergence in the GCMC simulations (Fig. S1 in the Electronic Supplementary Material (ESM)). Widom insertion calculations were performed using 1×10^5 cycles for RASPA2 and 5×10^5 steps for HULU. Note that a "cycle" in RASPA2 represents a sweep of MC moves, while a "step" in HULU refers to a single attempted move. GCMC, Widom insertion, and CMC (NVT ensemble) simulations were employed depending on the target property. In GCMC simulations, insertion, deletion, translation, rotation, and reinsertion moves were attempted with equal probabilities of 0.2 each. In CMC simulations, translation, rotation, and reinsertion moves were attempted with equal probabilities of 1/3. The fugacity was calculated using the Peng-Robinson equation of state. Unless otherwise specified, adsorption isotherms reported in this work correspond to excess adsorption, defined relative to the bulk gas phase. The ZIF-8 [46] framework and methane (CH_4) were treated as rigid in all MC simulations. Such a rigid treatment is widely adopted and has been shown to yield accurate results in a wide range of MC studies [14, 15, 19, 22, 47].

2.2 Molecular dynamics simulations

MD simulations were performed using Large-scale Atomic/Molecular Massively Parallel Simulator (LAMMPS) [48], Graphics Processing Units Molecular Dynamics (GPUMD) [49], and the Atomic Simulation Environment (ASE) [50] to generate reference structural properties, including radial distribution functions (RDFs) and spatial density distributions. Periodic boundary conditions were applied to all directions. The velocity-Verlet integration algorithm with a timestep of 1.0 fs was used to integrate the equations of motion. The Nosé–Hoover thermostat with a damping factor of 0.1 ps was used to control the temperature [51–53]. Notably, all frameworks and CH_4 molecules were treated as fully flexible during MD simulations. Energy minimization using the conjugate gradient algorithm was first performed to optimize the atomic positions. Subsequently, the MD simulations were carried out in the NVT ensemble by 20 ns, where the last 10 ns was analyzed. For bulk CH_4 simulations, systems containing 32, 64, or 128 CH_4 molecules were simulated in a cubic box of size 30 Å × 30 Å × 30 Å.

2.3 Density functional theory calculations

Density functional theory (DFT) using projector-augmented-wave (PAW) method [54] were implemented with the Vienna *ab initio* simulation package (VASP), version 6.1.0 [55]. The Perdew–Burke–Ernzerhof (PBE) exchange-correlation functional [56] and DFT-D3 dispersion correction with Becke–Johnson (BJ) damping function [57, 58] were applied. Gaussian smearing with a smearing width of 0.05 eV was utilized to perform calculations with an energy cutoff of 520 eV for the plane-wave basis set. The electronic convergence criteria was set to 10^{-6} eV. Brillouin zone sampling was restricted to the Γ-point. DFT calculations were used exclusively for single-point energy evaluations of Widom insertion configurations. The insertion energy (ΔE) was defined as

$$\Delta E = E_{\text{framework+gas}} - E_{\text{framework}} - E_{\text{gas}} \quad (1)$$

The gas-phase energy (E_{gas}) in Eq. (1) was calculated for an isolated CH_4 molecule in a sufficiently large vacuum box.

2.4 Empirical force fields and machine learning potentials

For simulations using empirical force fields, the ZIF-FF [59] force field was employed for ZIF-8, while the CH_4 was described by the TraPPE force field [60]. The van der Waals interactions were calculated with a cutoff of 14.0 Å and without tail corrections. All empirical force field calculations in HULU were implemented via a custom ASE calculator enabling single-point energy evaluations. The corresponding code is open-source and publicly available as described in the Data availability section.

Three MLP frameworks, MACE [32, 33], NEP [34–36], and ORB [38, 39], were investigated in this work. The following pre-trained foundation models were employed: MACE-Mat [61], NEP89 [62], and ORB v3 [39]. For MACE-Mat and ORB v3, long-range dispersion interactions were explicitly included via DFT-D3(BJ) corrections, added on-the-fly to the MLP-predicted energies using the torch-dftd library [63]. DFT-D3(BJ) corrections were not applied to NEP89, as dispersion interactions are inherently included in its training set.

For simulations involving MLPs, a 1 × 1 × 1 ZIF-8 unit cell was used for computational efficiency, whereas a 2 × 2 × 2 supercell was employed in empirical force field simulations to satisfy the minimum image convention.

2.5 Data analysis and visualization

Structural analyses, including RDFs and spatial density distributions, were performed using the MDAnalysis package [64, 65]. All reported quantities correspond to ensemble-averaged values accumulated over production steps (or production cycles in the case of RASPA2). Visualization of the simulation system was performed using OVITO [66].

HULU provides per-step outputs that record energy chang (ΔE) for each attempted MC move, enabling detailed statistical analyses in Section 3.4. With ΔE, the statistical weight of each configuration can be determined by the Boltzmann factor [67]

$$\mathrm{Bf}(\Delta E) = \mathrm{e}^{-\beta \Delta E} \tag{2}$$

where $\beta = 1/(RT)$, R is the gas constant, and T corresponds to temperature. The Boltzmann factor in Eq. (2) directly governs the acceptance probability of MC moves. For example, the acceptance probability of an insertion move in GCMC follows the Metropolis criterion [67]

$$P_{\mathrm{acc}} = \min\left[1, \frac{fV}{N+1}\mathrm{e}^{-\beta \Delta E}\right] \tag{3}$$

where f is the fugacity, V corresponds to the system volume, and N is the number of particles. Consequently, configurations with lower ΔE (larger Boltzmann weights) exhibit higher acceptance probabilities in GCMC, as described by Eq. (3), thereby increasing the predicted adsorption uptake.

Furthermore, thermodynamic properties that are directly comparable to experiments, such as Henry constant (K_{H}) and the heat of adsorption (Q_{st}) at infinite dilution, can be derived from Boltzmann-weighted averages of ΔE. These properties are evaluated using the Widom insertion method [68] as

$$Q_{\mathrm{st}} = -\frac{\langle \Delta E \mathrm{e}^{-\beta \Delta E}\rangle}{\langle \mathrm{e}^{-\beta \Delta E}\rangle} + RT \tag{4}$$

$$K_{\mathrm{H}} = \frac{V}{RTm}\langle \mathrm{e}^{-\beta \Delta E}\rangle \tag{5}$$

where m is the total system masses, and <·> denotes ensemble average.

Accordingly, differences in ΔE predicted by different MLPs yield distinct Boltzmann-weighted contributions and, consequently, thermodynamic properties (e.g., uptake and henry constants, see Eqs. (4) and (5)). To quantify these contributions, we compute the cumulative contribution of the Boltzmann factor as

$$C(\Delta E_k) = \frac{\sum_{i=1}^{k} \mathrm{e}^{-\beta \Delta E_i}}{\sum_{i=1}^{N} \mathrm{e}^{-\beta \Delta E_i}} \tag{6}$$

Note that the ΔE values in this work, obtained from Widom insertions or other MC moves (e.g., insertion attempts in GCMC), are discrete samples rather than a continuous variable. Consequently, the configuration with the lowest ΔE already accounts for a finite fraction of the total Boltzmann weight, leading to a non-zero initial value (Eq. (6)) of the cumulative contribution curves. These curves do not represent conventional probability cumulative distribution functions (CDFs), but rather Boltzmann-weighted cumulative contributions.

3 Results and discussion

3.1 Architecture and design philosophy of the HULU package

Most existing MC implementations are tightly coupled to specific force fields. For instance, widely used codes like RASPA2 are designed primarily for empirical potentials. To enable the application of MLPs in adsorption simulations, we developed a flexible MC framework, HULU, built on the ASE package [50]. As shown in Fig. 1, HULU integrates three core modules that cover essential adsorption simulation tasks: Widom insertion, GCMC, and CMC (NVT ensemble). These modules enable the direct calculation of key adsorption properties, including adsorption isotherms, heats of adsorption, and Henry constants, as well as the sampling of potential energy surfaces.

In HULU, the ASE energy calculator serves as a single-point energy evaluator. This design explicitly decouples MC sampling from energy evaluations, rendering the framework naturally compatible with MLP-based adsorption simulations. Notably, state-of-the-art MLPs such as ACE, DP, MACE, NEP, NequIP, and ORB already provide ASE-compatible interfaces [37, 69]. Following this modular philosophy, a typical workflow in HULU involves (Fig. 1): (i) specifying simulation parameters and initializing an ASE energy calculator; (ii) performing adsorption MC simulations (GCMC, Widom insertion, or CMC); and (iii) obtaining the ensemble averaged adsorption properties along with sampled configurations for post-analysis. Crucially, HULU requires only single-point energies for given configurations and is therefore independent on the underlying energy calculator, whether derived from MLPs, empirical force fields, or DFT, establishing it as a unified platform for multi-fidelity adsorption simulations (Fig. 1).

3.2 Validation against mainstream simulation packages

To validate the sampling reliability of HULU in the canonical (NVT) ensemble, we performed systematic benchmarks on two representative systems: CH_4 in both bulk phases and confined states within ZIF-8. Specifically, the radial distribution functions (RDFs) calculated by HULU, such as the C–C correlations for CH_4 were compared against results from the existing MC code RASPA2, as well as established MD engines (LAMMPS, ASE and GPUMD). All simulations were conducted at 313.15 K to ensure consistent sampling statistics between the MC and MD trajectories.

As shown in Fig. 2(a), the RDFs of bulk CH_4 predicted by HULU exhibit excellent agreement with those from MD simulations across all tested potentials, with a root-mean-square error (RMSE) as low as 0.030 for empirical FF performed with LAMMPS (Fig. 2(a)).

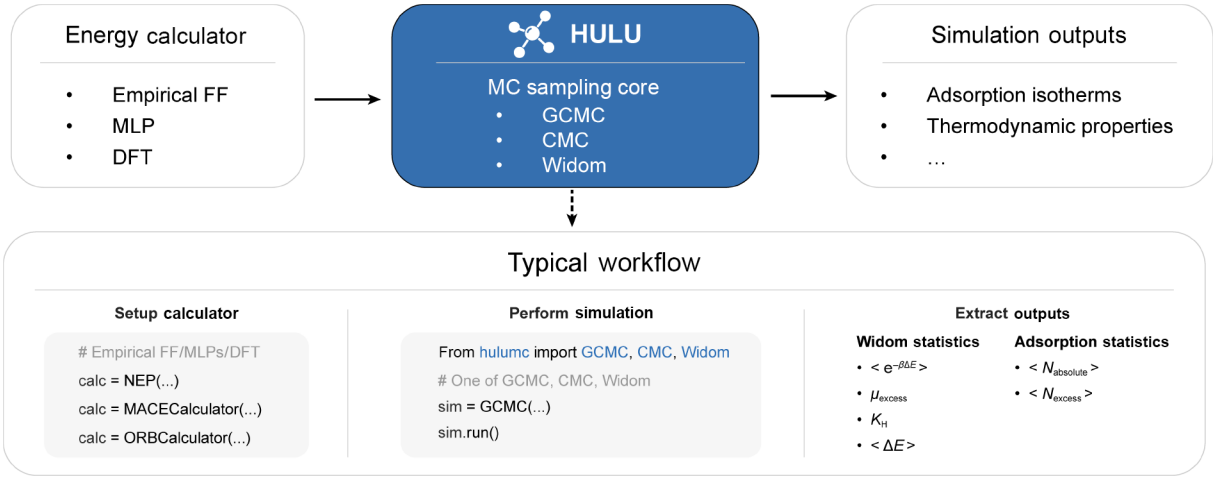

Figure 1 Overview of the HULU package and its typical workflow. HULU provides a unified MC sampling core interfaced with different energy calculators, including empirical FFs, MLPs, and DFT. The sampling core consists of three simulation modules, Widom insertion, GCMC, and CMC, covering the most common adsorption simulation tasks. A typical workflow includes calculator setup, simulation execution, and automated extraction of adsorption-related outputs. Widom insertion yields thermodynamic descriptors such as Boltzmann factor ($e^{-\beta\Delta E}$), excess chemical potential (μ_{excess}), Henry constant (K_H), and insertion energy (ΔE), while GCMC simulations provide adsorption statistics including absolute ($N_{absolute}$) and excess adsorption (N_{excess}). Angle brackets $\langle\cdot\rangle$ denote ensemble averages.

Consistent agreement was also observed at other CH_4 loadings (Fig. S2 in the ESM). In particular, the position and intensity of the first coordination peak at ~ 4.3 Å are accurately reproduced by HULU. This consistency holds true not only for empirical force fields but also for all three MLPs (MACE-Mat, NEP89, and ORB v3), confirming the robust implementation of MLP interfaces. More generally, the RDFs obtained from HULU are indistinguishable from those generated by widely used MD codes (LAMMPS, GPUMD, and ASE), confirming that HULU correctly samples configurations consistent with the Boltzmann distribution in the canonical ensemble. Beyond the structural validation, we further assessed the accuracy of thermodynamic properties predicted by HULU by benchmarking against RASPA2, using CH_4 adsorption in ZIF-8 as a representative system. Given that RASPA2 is limited to empirical potentials, simulations were performed using identical force fields (ZIF-FF for the framework and TraPPE for CH_4), implemented in HULU via an in-house ASE calculator (Section 2.4). As shown in Fig. 2(b), the adsorption isotherms calculated by HULU achieve excellent agreement with RASPA2 results across the entire pressure range. Quantitatively, the predicted heats of adsorption differ by less than 0.10%, and the Henry constants deviate less than 0.65% (Fig. 2(c)). To elucidate the microscopic adsorption mechanism, spatial density distributions of CH_4 were analyzed at a fixed loading of 7 CH_4/unit cell (corresponding to absolute adsorption at 10 bar). Configurations were sampled via canonical MC simulations (using HULU and RASPA2) and MD simulations (using LAMMPS). Remarkably, HULU reproduces the distinct preferential localization of CH_4 near the six-membered ring (6MR) and four-membered ring (4MR) windows of ZIF-8, yielding patterns indistinguishable from the patterns generated by RASPA2 and LAMMPS (Fig. 2(d)). These adsorption sites are also consistent with experimental observations [19]. Collectively, these results provide rigorous validation for both the macroscopic thermodynamic properties and microscopic behaviors predicted by HULU.

3.3 Enabling MLP-driven adsorption MC simulations

Having established the sampling accuracy of HULU against standard benchmarks (RASPA2, GPUMD, and LAMMPS), we now leverage its decoupled architecture to address a critical capability gap: performing adsorption MC simulations using MLPs, a task currently unsupported by mainstream adsorption codes.

We focused on ZIF-8/CH_4 system, a prototypical benchmark extensively studied in both experiments and computations (Fig. 3(a)) [15, 19, 47, 70, 71]. Three representative pre-trained foundation MLP models were evaluated: NEP89, MACE-Mat, and ORB v3. NEP89 and ORB v3 represent the latest iterations of their respective frameworks (until November 2025), while MACE-Mat remains as the officially recommended and widely adopted version. In our GCMC simulations, we explicitly added the DFT-D3(BJ) dispersion corrections to simulations using MACE-Mat and ORB v3. This correction was omitted for NEP89, as it was trained on datasets that inherently include D3 dispersion energies. As shown in Fig. 3(b), dispersion interactions play a pivotal role in accurately describing CH_4 adsorption in ZIF-8.

Without applying DFT-D3(BJ) corrections, both MACE-Mat and ORB v3 predict nearly negligible adsorption. These models are trained on datasets generated using the PBE functional [56], a semi-local approximation that does not adequately capture long-range dispersion interactions [38], thereby underestimating the CH_4-ZIF-8 interactions. However, even with dispersion corrections applied, significant discrepancies persist among the three models. Specifically, NEP89 provides the most accurate description, capturing both the isotherm shape and capacity, with an average deviation of less than 10% from experimental data. In contrast, MACE-Mat captures the overall trend but slightly overestimates the adsorption amount, with an average deviation exceeding 100%. Notably, we screened multiple pre-trained MACE foundation models (differing in training data, level of theory and model size), and found that MACE-Mat offers the best performance (Fig. S3 in the ESM). Conversely, ORB v3 exhibits a drastic overestimation, predicting a capacity 373.8% higher than the experimental value at pressure as low as 0.2 bar. For reference, the standard empirical force field yields a slight overestimation of the experimental capacity.

Given that gas–gas interactions are relatively weak in the low-loading regime [72, 73], the observed deviation in isotherms may be primarily attributed to the differences in the framework-guest (ZIF-

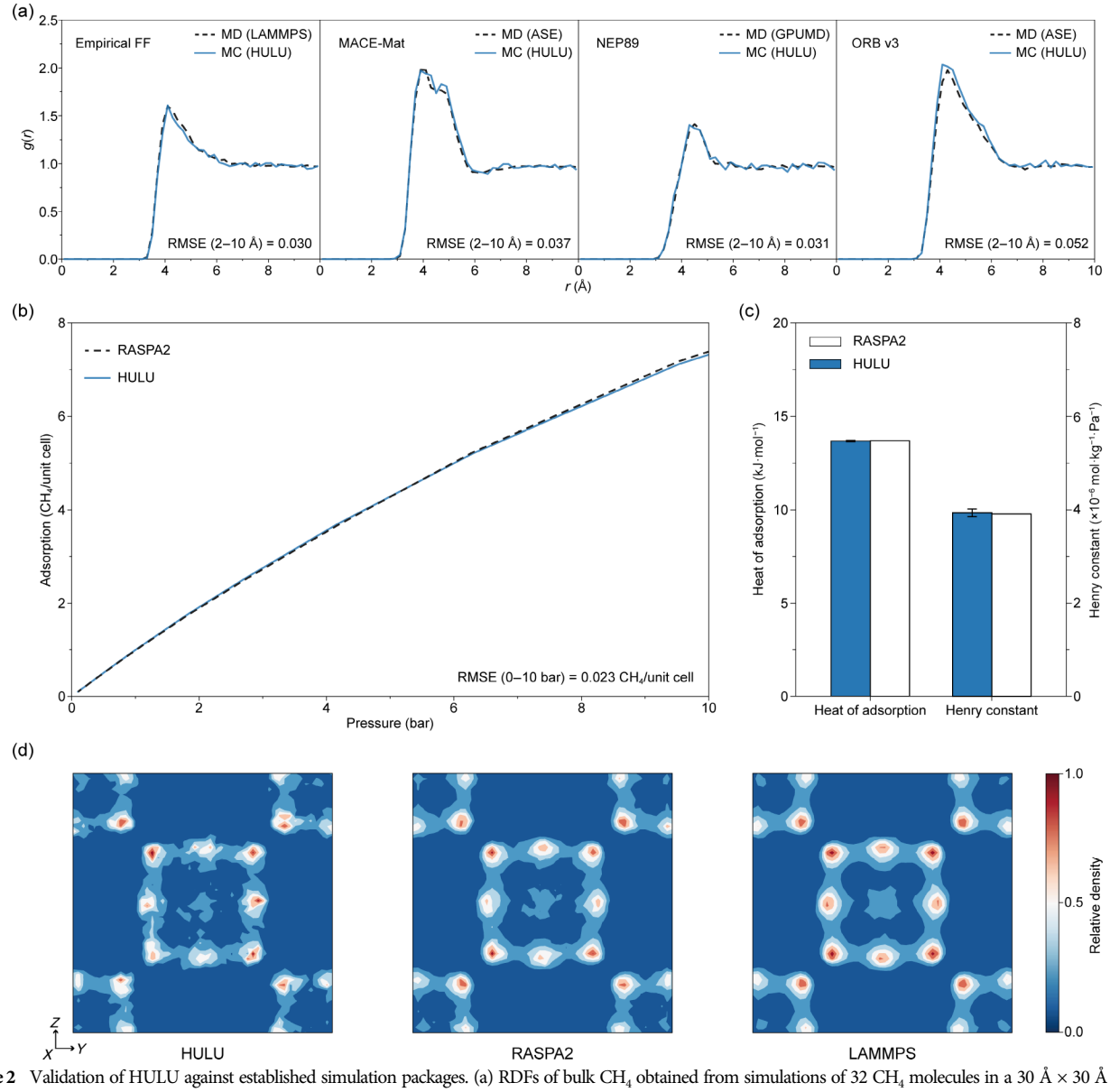

Figure 2 Validation of HULU against established simulation packages. (a) RDFs of bulk CH_4 obtained from simulations of 32 CH_4 molecules in a 30 Å × 30 Å × 30 Å cubic box using both empirical FFs and MLPs. Results from MC simulations with HULU were compared with MD simulations performed using LAMMPS, GPUMD and ASE. Results for other CH_4 loadings were provided in Fig. S2 in the ESM. (b) Adsorption isotherm of CH_4 in ZIF-8 computed using HULU and compared with results from RASPA2. (c) Heats of adsorption and Henry constants of CH_4 in ZIF-8 obtained from HULU and RASPA2. Error bars represent standard deviations, calculated from five-block averaging of Widom insertion data. Those for RASPA2 are too small to be visible. (d) Equilibrium density distributions of CH_4 within ZIF-8 predicted by HULU, RASPA2, and LAMMPS. The density distributions were sampled from canonical (NVT) trajectories at a loading of 7 CH_4/unit cell.

8-CH_4) interactions predicted by each MLP. To quantify these interactions, we calculated the Henry constants (K_H) for each model (Fig. 3(c)). Consistent with the isotherm trends, NEP89 yields a Henry constant of K_H = 2.55 × 10^{-6} mol·kg^{-1}·Pa^{-1}, which is remarkably close to the experimental value (2.24 × 10^{-6} mol·kg^{-1}·Pa^{-1}). In sharp contrast, ORB v3 predicts a Henry constant of 5.67 × 10^{-5} mol·kg^{-1}·Pa^{-1}, overestimating the experimental value by more than one order of magnitude. Both MACE-Mat and the empirical force field yielded moderately larger Henry constants, consistent with their tendency to overestimate CH_4 uptakes compared to experiment (Fig. 3(b)). These results provide a straightforward explanation for the discrepancies in the adsorption isotherms: over-binding between the framework and guest molecules leads to artificially enhanced adsorption. However, since the Henry constant strictly characterizes the infinite-dilution limit, a more comprehensive analysis covering the full loading will be presented in Section 3.4.

To further analyze the microscopic behavior predicted by the three MLPs, we generated 400 representative configurations via Widom insertion and evaluated their insertion energies (ΔE) at the benchmark PBE + D3(BJ) level. Low-energy regions are identified near both the 6MR and 4MR windows of ZIF-8, in good agreement with experimentally reported adsorption sites [19]. Conversely, relatively high ΔE values were observed at the center of the 6MR window. This energy barrier arises from steric hindrance, given that the kinetic diameter of CH_4 (~ 3.8 Å) [74] exceeds the nominal aperture size of ZIF-8 (~ 3.4 Å) [46]. The spatial density distributions of CH_4 predicted by the three MLPs (Fig. 3(e)) exhibit

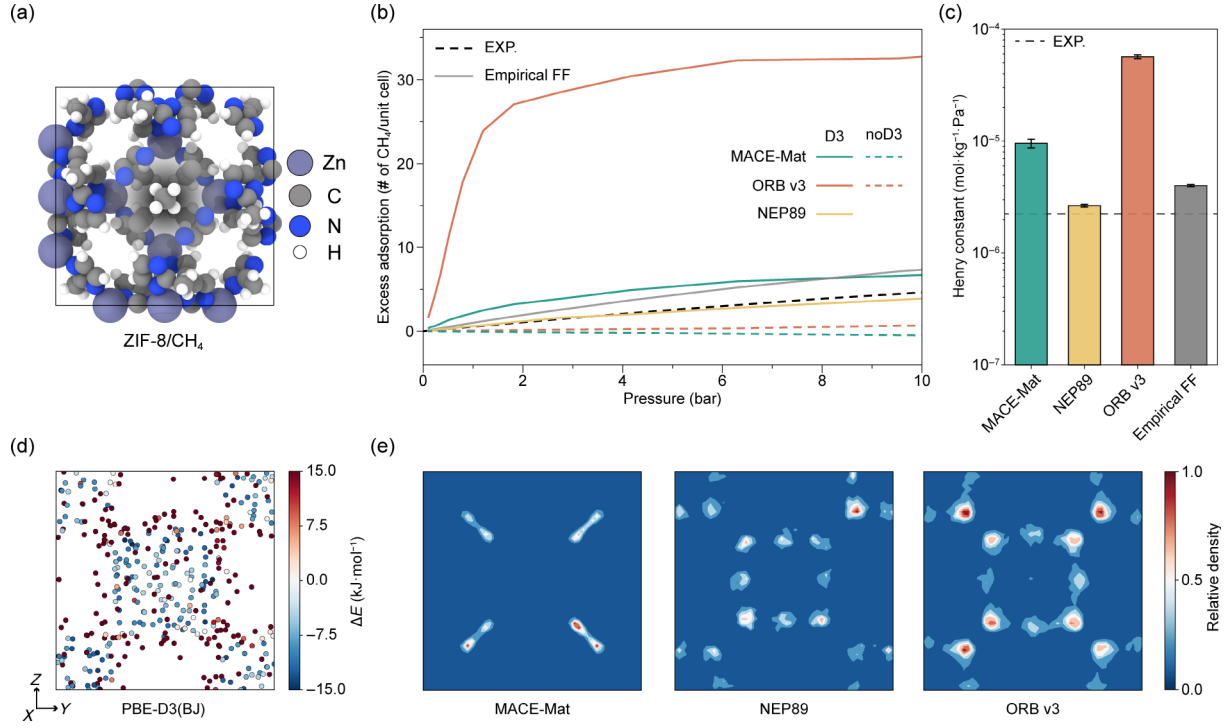

Figure 3 Comparison of CH_4 adsorption in ZIF-8 using three MLPs. (a) Simulation system of CH_4 adsorption in ZIF-8. (b) CH_4 adsorption isotherms predicted by three MLPs, MACE-Mat, NEP89, and ORB v3, compared with results from experiment and an empirical force field. The adsorption reported here corresponds to excess adsorption. (c) Henry constants of CH_4 in ZIF-8 calculated by Widom insertion using three MLPs. Error bars represent standard deviations, calculated from five-block averaging of Widom insertion data. The experimental Henry constant [75] is shown for reference. (d) Distribution of Widom insertion energies (ΔE) evaluated at the PBE-D3(BJ) level. (e) Spatial density distributions of CH_4 in ZIF-8 predicted by MACE-Mat, NEP89, and ORB v3, highlighting differences in preferential adsorption sites. These density distributions were obtained from canonical MC simulations using a single CH_4 molecule, corresponding to the infinite-dilution situation.

pronounced differences. MACE-Mat only captures the adsorption site near the 6MR, while both NEP89 and ORB v3 identify adsorption sites near both the 6MR and 4MR. However, ORB v3 exhibits a highly localized distribution, indicating excessively strong host–guest interactions. This observation is consistent with its severely overestimated uptakes (Fig. 3(b)) and Henry constant (Fig. 3(c))

3.4 Origins of performance discrepancies among MLPs

As previously discussed, NEP89 yields adsorption isotherms in close agreement with experiment, whereas MACE-Mat and ORB v3 overestimate CH_4 uptake in ZIF-8. This discrepancy motivates us to further examine the interaction energies predicted by the three models.

To quantify these interaction energies, we compared Widom insertion energies (ΔE) predicted by the MLPs against those obtained from benchmark DFT calculations. With dispersion corrections applied on MACE-Mat and ORB v3, all three models exhibit moderate deviations from PBE-D3(BJ) (Fig. 4(a)). However, when DFT-D3(BJ) dispersion corrections were removed, the deviations predicted by both ORB v3 and MACE-Mat increased substantially (Fig. S4 in the ESM), indicating weaker binding. In particular, the RMSE for MACE-Mat increases dramatically from 5.47 to 13.70 kJ·mol^{-1}, indicating a strong underestimation of host–guest interactions.

To further investigate the influence of dispersion interactions, Henry constants were recalculated without applying DFT-D3(BJ) to MACE and ORB v3. As shown in Fig. S5 in the ESM, the Henry constants obtained without DFT-D3(BJ) corrections are not only markedly lower than the dispersion-corrected values, but also significantly underestimated relative to the experimental values. This underestimation is directly reflected in the adsorption isotherms, i.e., the nearly negligible CH_4 uptake predicted by MACE and ORB v3 in the absence of dispersion corrections (Fig. 3(b)).

Although the critical role of dispersion corrections has been established, analyzing insertion energies (ΔE) alone is insufficient to fully explain the pronounced differences in adsorption behavior predicted by the three models. In statistical mechanics, adsorption properties are governed by Boltzmann-weighted statistics, where a small subset of configurations may dominate the ensemble average [67]. This contribution can be quantified by the Boltzmann factor, $e^{-\beta\Delta E}$. As shown in Fig. 4(b), NEP89 reproduces the DFT-calculated Boltzmann weighted distribution. In contrast, MACE-Mat and ORB v3 exhibit disproportionately high contributions from low-energy states, leading to systematic overestimation of adsorption properties (e.g., CH_4 uptake and Henry constants).

Notably, for MACE-Mat, only 2 out of 200 Widom insertion configurations account for approximately 80% of the total Boltzmann-weighted sum. As discussed earlier (Fig. 3(e)), this artifact stems from a specific overestimation of interactions near 6MR window. Similarly, for ORB v3, the weighted probability distribution is systematically shifted toward lower ΔE values relative to PBE-D3(BJ) benchmark, resulting in inflated adsorption statistics across the board.

Crucially, in GCMC simulations, differences in the ΔE distributions predicted by the three MLPs lead to distinct Boltzmann-weighted statistics, which directly dictate the acceptance probabilities of insertion and deletion moves. Due to the exponential nature of the Metropolis acceptance rule [67], even

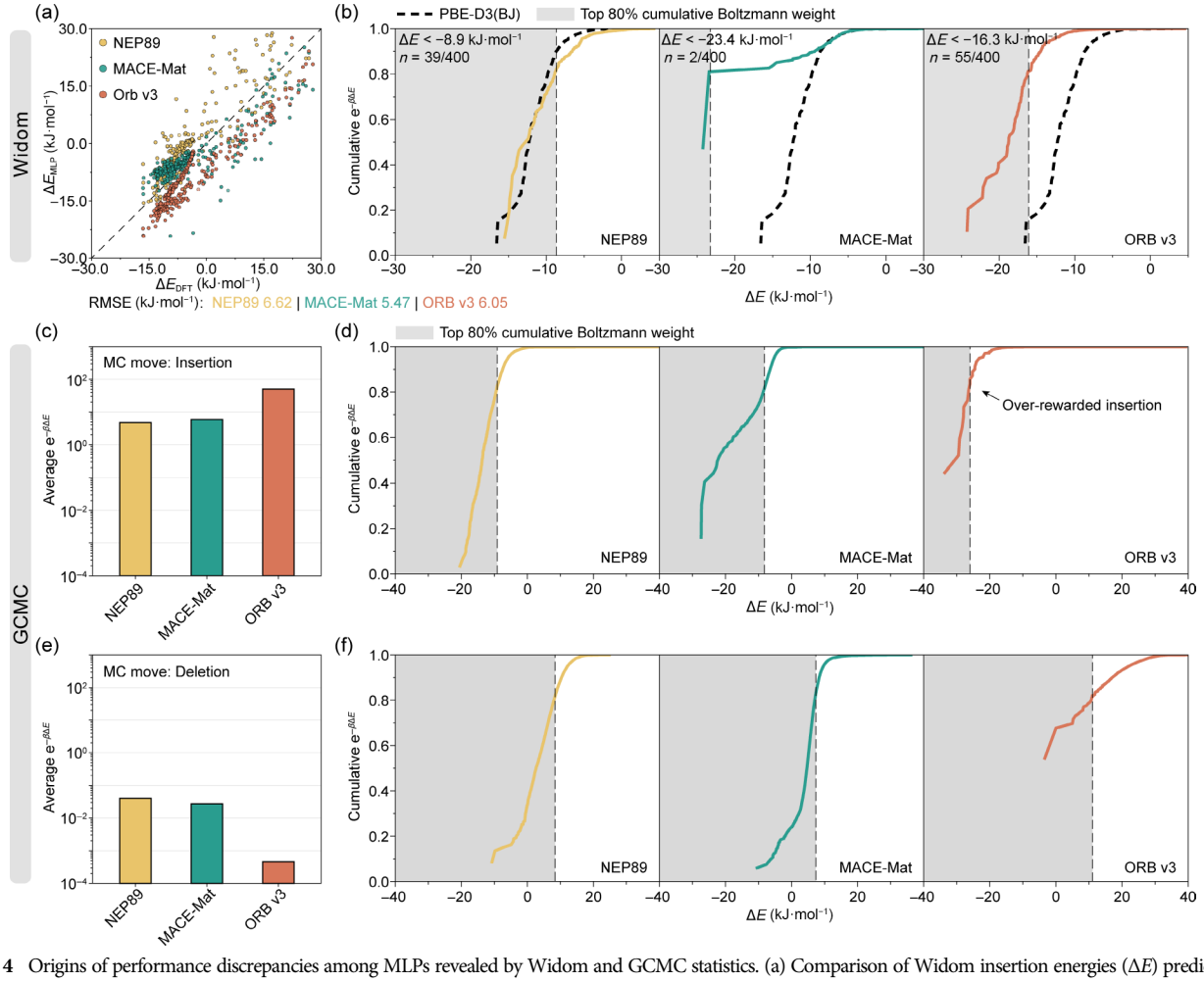

Figure 4 Origins of performance discrepancies among MLPs revealed by Widom and GCMC statistics. (a) Comparison of Widom insertion energies (ΔE) predicted by MLPs with reference PBE-D3(BJ) calculations for CH_4 in ZIF-8, with the corresponding RMSE values. (b) Cumulative Boltzmann-weighted contributions, $e^{-\beta\Delta E}$. (c) Average Boltzmann factors $\langle e^{-\beta\Delta E} \rangle$ for insertion moves. (d) Cumulative Boltzmann-weighted contributions $e^{-\beta\Delta E}$ for GCMC insertion moves. (e) Average Boltzmann factors $\langle e^{-\beta\Delta E} \rangle$ for deletion moves. (f) Cumulative Boltzmann-weighted contributions $e^{-\beta\Delta E}$ for GCMC deletion moves. In panels (c) and (e), the average Boltzmann factors quantify the effective energetic favorability of particle insertion and deletion in GCMC simulations. In panels (b), (d) and (f), the shaded region denotes the ΔE interval contributing to 80% of cumulative Boltzmann weight sampled from Widom insertion or GCMC simulations. These curves start from non-zero values because they are constructed from discretely sampled ΔE values (see "Computational details" section for details).

minor energetic discrepancies are significantly amplified. For example, under identical simulation conditions (same temperature, pressure, and empty framework), a shift of 10 kJ·mol^{-1} in ΔE can lead to up to ~ 5000% change in the acceptance probability (Eq. (3)). As shown in Fig. 4(c), ORB v3 yield systematically larger Boltzmann factors for insertion moves by predicting more negative ΔE values (Fig. 4(d)). Concurrently, it imposes higher energy barrier that suppresses particle removal (Figs. 4(e) and 4(f)). This asymmetry between insertion and deletion acceptance probabilities biases the sampling toward higher loadings, directly resulting in the overestimated adsorption isotherms. MACE-Mat exhibits behavior intermediate between NEP89 and ORB v3, yielding adsorption uptakes that fall between the two.

Overall, the divergence in adsorption predictions among the MLPs can be traced to the exponential amplification of small ΔE biases through Boltzmann-weighted MC sampling. A fundamental limitation is that most MLPs employ relatively short interaction cutoffs (typically 5–7 Å) [76], rendering them inherently incapable of capturing long-range dispersion interactions that are essential for adsorption. Consequently, we highlight that explicitly incorporating long-range dispersion interactions (e.g., DFT-D3) [77] is not merely an enhancement but a necessity for accurate MLP-based adsorption simulations.

4 Conclusion

In this work, we developed HULU, a flexible MC package for adsorption simulations, allowing for the seamless integration of empirical force fields, DFT, and MLPs. Built on the ASE, HULU implements Widom insertion, GCMC, and CMC modules, enabling the calculation of a comprehensive suite of adsorption properties. Extensive validation confirms that HULU yielded RDFs, adsorption isotherms, and thermodynamic descriptors that are in excellent agreement with both MD simulations (using MLPs and empirical FFs) and established adsorption simulation codes (using empirical FFs only).

Leveraging HULU as a versatile platform, we systematically evaluated the performance of three representative MLPs (NEP89, MACE-Mat and ORB v3) for CH_4 adsorption in ZIF-8, using their latest recommended pre-trained foundation models. Pronounced performance differences were observed: NEP89 yields adsorption

isotherms consistent with experimental trends, whereas MACE-Mat slightly overestimates the adsorption capacity, and ORB v3 exhibits substantial overestimation. These discrepancies were traced to differences in the predicted framework-guest interactions, as indicated by Henry constants. Through a detailed analysis of Widom insertion energies, we demonstrated that while NEP89 accurately reproduces the Boltzmann-dominant energy contributions (verified at the PBE-D3(BJ) level), the other models deviate. Specifically, MACE-Mat is disproportionately biased by a small number of low-energy configurations, while ORB v3 shows a systematic overestimation of framework–guest interaction energies. Crucially, our results highlight that an accurate description of dispersion interactions is a prerequisite for reliable MLP-based adsorption simulations. Collectively, the HULU package and the mechanistic insights provided here establish a solid foundation for extending high-accuracy machine learning potentials to the screening and design of nanoporous materials.

Electronic Supplementary Material: Supplementary material (additional figures on GCMC convergence, RDFs, adsorption isotherms, Widom insertion energies, and Henry constants) is available in the online version of this article at https://doi.org/10.26599/NR.2026.94908548.

Data availability

All data needed to support the conclusions in the paper are presented in the manuscript and the Electronic Supplementary Material. Additional data related to this paper may be requested from the corresponding author upon request.

Acknowledgements

We gratefully acknowledge the support from the National Natural Science Foundation of China (No. U23A20115), Science and Technology Key Project of Guangdong Province (No. 2025B0101060003), the Natural Science Foundation of Guangdong Province (Nos. 2024A1515012725 and 2024A1515012724), Guangzhou Municipal Science and Technology Project (No. 2024A04J6251), State Key Laboratory of Advanced Papermaking and Paper-based Materials (Nos. 2024ZD03 and 2025PT02), Fundamental Research Funds for the Central Universities (No. 2025ZYGXZR023), and the National Natural Science Foundation of China (No. 22078104). The simulations in this work were supported by the Open Source Supercomputing Center of S-A-I.

Declaration of competing interest

All the contributing authors report no conflict of interests in this work.

Author contribution statement

X. T. C.: Conceptualization, methodology, software, data curation, formal analysis, validation, visualization, writing – original draft. Y. X. W.: Data curation, formal analysis. L. B. L.: Conceptualization, supervision, funding acquisition, writing – review & editing, project administration. L. J. L.: Data curation, formal analysis. P. H. Y.: Conceptualization, methodology, writing – review & editing. Y. Y. W.: Conceptualization, supervision, writing – review & editing. All the authors have approved the final manuscript.

Use of AI statement

None.

References

[1] Peng, X. W.; Zhang, H.; Zeng, H. B. Covalent organic framework materials with advanced topologies for efficient methane adsorption. *Sci. China Mater.* **2025**, *68*, 1298–1299.

[2] Zhong, Y. L.; Fang, P. H.; Zhai, M. Y.; Low, Z.; Chen, Z. J. Complexity in order: High-porosity multicomponent metal-organic frameworks for clean energy gas storage. *J. Am. Chem. Soc.* **2025**, *147*, 45377–45385.

[3] Gunathilake, C.; Soliman, I.; Panthi, D.; Tandler, P.; Fatani, O.; Ghulamullah, N. A.; Marasinghe, D.; Farhath, M.; Madhujith, T.; Conrad, K. et al. A comprehensive review on hydrogen production, storage, and applications. *Chem. Soc. Rev.* **2024**, *53*, 10900–10969.

[4] Zhang, X. J.; Wu, T.; Liu, B. Y.; Li, G.; Lu, A. H. Efficient hydrogen/carbon dioxide separation by magnifying their diffusion difference in carbon molecular sieve membranes. *Nano Res.* **2025**, *18*, 94907322.

[5] Wan, M. L.; Liu, Y. S.; Chen, X.; Arsakay, M.; Wei, F.; Ruoff, R. S.; Song, B.; Shen, B. Y. Pore size engineering of carbon-modulated zeolite framework for controllable selective adsorption of small gas molecules. *Nano Res.* **2025**, *18*, 94907770.

[6] Cui, J. Y.; Zhang, Z. Q.; Yang, L. F.; Hu, J. B.; Jin, A. Y.; Yang, Z. L.; Zhao, Y.; Meng, B.; Zhou, Y.; Wang, J. et al. A molecular sieve with ultrafast adsorption kinetics for propylene separation. *Science* **2024**, *383*, 179–183.

[7] Li, L. B.; Lin, R. B.; Krishna, R.; Li, H.; Xiang, S. C.; Wu, H.; Li, J. P.; Zhou, W.; Chen, B. L. Ethane/ethylene separation in a metal-organic framework with iron-peroxo sites. *Science* **2018**, *362*, 443–446.

[8] Zhao, D. F.; Lin, J.; Li, R. S.; Xu, X. M.; Hu, F. J.; Wang, Z. K.; Huang, X. B.; Wang, G. Nickel-mediated formation of stable frustrated Lewis pairs in rare earth MOFs for dicyclopentadiene hydrogenation. *Sci. China Mater.* **2025**, *68*, 1880–1892.

[9] Zheng, X. R.; Wang, Y. C.; Guan, J. P.; Liu, X.; Bai, Y.; Chen, Y. B.; Yang, P. Y.; Zhang, J.; Ou, H. Z.; Wang, M. et al. High-loading inducing Fe-dimer on carbon nitride promotes the generation of $\cdot O_2^-$. *Adv. Powder Mater.* **2025**, *4*, 100308.

[10] Kim, H.; Yang, S.; Rao, S. R.; Narayanan, S.; Kapustin, E. A.; Furukawa, H.; Umans, A. S.; Yaghi, O. M.; Wang, E. N. Water harvesting from air with metal-organic frameworks powered by natural sunlight. *Science* **2017**, *356*, 430–434.

[11] Hanikel, N.; Pei, X. K.; Chheda, S.; Lyu, H.; Jeong, W.; Sauer , J.; Gagliardi, L.; Yaghi, O. M. Evolution of water structures in metal-organic frameworks for improved atmospheric water harvesting. *Science* **2021**, *374*, 454–459.

[12] Goeminne, R.; van Speybroeck, V. *Ab initio* predictions of adsorption in flexible metal-organic frameworks for water harvesting applications. *J. Am. Chem. Soc.* **2025**, *147*, 3615–3630.

[13] Daglar, H.; Gulbalkan, H. C.; Aksu, G. O.; Keskin, S. Computational simulations of metal-organic frameworks to enhance adsorption applications. *Adv. Mater.* **2025**, *37*, 2405532.

[14] Lim, Y.; Park, H.; Walsh, A.; Kim, J. Accelerating CO_2 direct air capture screening for metal-organic frameworks with a transferable machine learning force field. *Matter* **2025**, *8*, 102203.

[15] Li, L. B.; Duan, Y. F.; Liao, S. W.; Ke, Q.; Qiao, Z. W.; Wei, Y. Y. Adsorption and separation of propane/propylene on various ZIF-8 polymorphs: Insights from GCMC simulations and the ideal adsorbed solution theory (IAST). *Chem. Eng. J.* **2020**, *386*, 123945.

[16] Wan, H.; Fang, Y.; Hu, M.; Guo, S. Y.; Sui, Z. Q.; Huang, X. S.; Liu, Z. L.; Zhao, Y.; Liang, H.; Wu, Y. F. et al. Interpretable machine-

learning and big data mining to predict the CO_2 separation in polymer-MOF mixed matrix membranes. *Adv. Sci.* **2025**, *12*, 2405905.
[17] Qiao, Z. W.; Li, L. F.; Li, S. H.; Liang, H.; Zhou, J.; Snurr, R. Q. Molecular fingerprint and machine learning to accelerate design of high-performance homochiral metal-organic frameworks. *AIChE J.* **2021**, *67*, e17352.
[18] Lamaire, A.; Wieme, J.; Vandenhaute, S.; Goeminne, R.; Rogge, S. M. J.; van Speybroeck, V. Water motifs in zirconium metal-organic frameworks induced by nanoconfinement and hydrophilic adsorption sites. *Nat. Commun.* **2024**, *15*, 9997.
[19] Hobday, C. L.; Woodall, C. H.; Lennox, M. J.; Frost, M.; Kamenev, K.; Düren, T.; Morrison, C. A.; Moggach, S. A. Understanding the adsorption process in ZIF-8 using high pressure crystallography and computational modelling. *Nat. Commun.* **2018**, *9*, 1429.
[20] Shi, Z. N.; Liao, L. J.; Peng, S. J.; Wei, Y. Y.; Li, L. B. Computational screening of covalent organic frameworks for He purification with adsorption or membrane separation. *Green Energy Environ.* **2025**, *10*, 2143–2155.
[21] Wang, Z. H.; Zhou, T. Computer-aided metal-organic framework screening and design approaches toward efficient carbon capture processes. *Mol. Syst. Des. Eng.* **2025**, *10*, 1005–1023.
[22] Zhao, G. B.; Brabson, L. M.; Chheda, S.; Huang, J.; Kim, H.; Liu, K. H.; Mochida, K.; Pham, T. D.; Prerna; Terrones, G. G. et al. CoRE MOF DB: A curated experimental metal-organic framework database with machine-learned properties for integrated material-process screening. *Matter* **2025**, *8*, 102140.
[23] Kulichenko, M.; Nebgen, B.; Lubbers, N.; Smith, J. S.; Barros, K.; Allen, A. E. A.; Habib, A.; Shinkle, E.; Fedik, N.; Li, Y. W. et al. Data generation for machine learning interatomic potentials and beyond. *Chem. Rev.* **2024**, *124*, 13681–13714.
[24] Fosu, E. A.; Yang, J. D. Machine-made chemistry. *Nat. Rev. Chem.* **2025**, *9*, 806.
[25] Jacobs, R.; Morgan, D.; Attarian, S.; Meng, J.; Shen, C.; Wu, Z. H.; Xie, C. Y.; Yang, J. H.; Artrith, N.; Blaiszik, B. et al. A practical guide to machine learning interatomic potentials-status and future. *Curr. Opin. Solid State Mater. Sci.* **2025**, *35*, 101214.
[26] Drautz, R. Atomic cluster expansion for accurate and transferable interatomic potentials. *Phys. Rev. B* **2019**, *99*, 014104.
[27] Dusson, G.; Bachmayr, M.; Csányi, G.; Drautz, R.; Etter, S.; van der Oord, C.; Ortner, C. Atomic cluster expansion: Completeness, efficiency and stability. *J. Comput. Phys.* **2022**, *454*, 110946.
[28] Witt, W. C.; van der Oord, C.; Gelžinytė, E.; Järvinen, T.; Ross, A.; Darby, J. P.; Ho, C. H.; Baldwin, W. J.; Sachs, M.; Kermode, J. et al. ACEpotentials.jl: A Julia implementation of the atomic cluster expansion. *J. Chem. Phys.* **2023**, *159*, 164101.
[29] Wang, H.; Zhang, L. F.; Han, J. Q.; E, W. N. DeePMD-kit: A deep learning package for many-body potential energy representation and molecular dynamics. *Comput. Phys. Commun.* **2018**, *228*, 178–184.
[30] Zeng, J. Z.; Zhang, D.; Lu, D. H.; Mo, P. H.; Li, Z. Y.; Chen, Y. X.; Rynik, M.; Huang, L. A.; Li, Z. Y.; Shi, S. C. et al. DeePMD-kit v2: A software package for deep potential models. *J. Chem. Phys.* **2023**, *159*, 054801.
[31] Zeng, J. Z.; Zhang, D.; Peng, A. Y.; Zhang, X. Y.; He, S. S.; Wang, Y.; Liu, X. Z.; Bi, H. R.; Li, Y. F.; Cai, C. et al. DeePMD-kit v3: A multiple-backend framework for machine learning potentials. *J. Chem. Theory Comput.* **2025**, *21*, 4375–4385.
[32] Batatia, I.; Kovács, D. P.; Simm, G. N. C.; Ortner, C.; Csányi, G. MACE: Higher order equivariant message passing neural networks for fast and accurate force fields. In *Proceedings of the 36th Conference on Neural Information Processing Systems*, New Orleans, USA, 2022.
[33] Batatia, I.; Batzner, S.; Kovács, D. P.; Musaelian, A.; Simm, G. N. C.; Drautz, R.; Ortner, C.; Kozinsky, B.; Csányi, G. The design space of E(3)-equivariant atom-centered interatomic potentials. *arXiv:* **2205**, *06643*, 2022.
[34] Song, K. K.; Zhao, R.; Liu, J. H.; Wang, Y. Z.; Lindgren, E.; Wang, Y.; Chen, S. D.; Xu, K.; Liang, T.; Ying, P. H. et al. General-purpose machine-learned potential for 16 elemental metals and their alloys. *Nat. Commun.* **2024**, *15*, 10208.
[35] Fan, Z. Y.; Zeng, Z. Z.; Zhang, C. Z.; Wang, Y. Z.; Song, K. K.; Dong, H. K.; Chen, Y.; Ala-Nissila, T. Neuroevolution machine learning potentials: Combining high accuracy and low cost in atomistic simulations and application to heat transport. *Phys. Rev. B* **2021**, *104*, 104309.
[36] Fan, Z. Y.; Wang, Y. Z.; Ying, P. H.; Song, K. K.; Wang, J. J.; Wang, Y.; Zeng, Z. H.; Xu, K.; Lindgren, E.; Rahm, J. M. et al. GPUMD: A package for constructing accurate machine-learned potentials and performing highly efficient atomistic simulations. *J. Chem. Phys.* **2022**, *157*, 114801.
[37] Tan, C. W.; Descoteaux, M. L.; Kotak, M.; de Miranda Nascimento, G.; Kavanagh, S. R.; Zichi, L.; Wang, M. H.; Saluja, A.; Hu, Y. R.; Smidt, T. et al. High-performance training and inference for deep equivariant interatomic potentials. *arXiv:* **2504**, *16068*, 2025.
[38] Neumann, M.; Gin, J.; Rhodes, B.; Bennett, S.; Li, Z. Y.; Choubisa, H.; Hussey, A.; Godwin, J. Orb: A fast, scalable neural network potential. *arXiv:* **2410**, *22570*, 2024.
[39] Rhodes, B.; Vandenhaute, S.; Šimkus, V.; Gin, J.; Godwin, J.; Duignan, T.; Neumann, M. Orb-v3: Atomistic simulation at scale. *arXiv:* **2504**, *06231*, 2025.
[40] Ying, P. H.; Qian, C.; Zhao, R.; Wang, Y. Z.; Xu, K.; Ding, F.; Chen, S. D.; Fan, Z. Y. Advances in modeling complex materials: The rise of neuroevolution potentials. *Chem. Phys. Rev.* **2025**, *6*, 011310.
[41] Yang, Y. H.; Wang, Y.; Liu, Y. A.; Keskin, S.; Jiang, Z. Y. Modeling gas transport in organic molecular sieve membranes. *AIChE J.* **2026**, *72*, e70042.
[42] Dubbeldam, D.; Calero, S.; Ellis, D. E.; Snurr, R. Q. RASPA: Molecular simulation software for adsorption and diffusion in flexible nanoporous materials. *Mol. Simul.* **2016**, *42*, 81–101.
[43] Shah, J. K.; Marin-Rimoldi, E.; Mullen, R. G.; Keene, B. P.; Khan, S.; Paluch, A. S.; Rai, N.; Romanielo, L. L.; Rosch, T. W.; Yoo, B. et al. Cassandra: An open source Monte Carlo package for molecular simulation. *J. Comput. Chem.* **2017**, *38*, 1727–1739.
[44] Gupta, A.; Chempath, S.; Sanborn, M. J.; Clark, L. A.; Snurr, R. Q. Object-oriented programming paradigms for molecular modeling. *Mol. Simul.* **2003**, *29*, 29–46.
[45] Wilson, W. N.; Bharadwaj, V. S.; Rai, N. Python library for monte carlo simulations with *ab initio* and machine-learned interatomic potentials. *J. Chem. Theory Comput.* **2025**, *21*, 10131–10141.
[46] Park, K. S.; Ni, Z.; Côté, A. P.; Choi, J. Y.; Huang, R. D.; Uribe-Romo, F. J.; Chae, H. K.; O'Keeffe, M.; Yaghi, O. M. Exceptional chemical and thermal stability of zeolitic imidazolate frameworks. *Proc. Natl. Acad. Sci. USA* **2006**, *103*, 10186–10191.
[47] Verploegh, R. J.; Nair, S.; Sholl, D. S. Temperature and loading-dependent diffusion of light hydrocarbons in ZIF-8 as predicted through fully flexible molecular simulations. *J. Am. Chem. Soc.* **2015**, *137*, 15760–15771.
[48] Thompson, A. P.; Aktulga, H. M.; Berger, R.; Bolintineanu, D. S.; Brown, W. M.; Crozier, P. S.; in 't Veld, P. J.; Kohlmeyer, A.; Moore, S. G.; Nguyen, T. D. et al. LAMMPS—A flexible simulation tool for particle-based materials modeling at the atomic, meso, and continuum scales. *Comput. Phys. Commun.* **2022**, *271*, 108171.
[49] Xu, K.; Bu, H. K.; Pan, S. N.; Lindgren, E.; Wu, Y. C.; Wang, Y.; Liu, J. H.; Song, K. K.; Xu, B.; Li, Y. F. et al. GPUMD 4.0: A high-performance molecular dynamics package for versatile materials simulations with machine-learned potentials. *MGE Adv.* **2025**, *3*, e70028.
[50] Hjorth Larsen, A.; Jørgen Mortensen, J.; Blomqvist, J.; Castelli, I. E.; Christensen, R.; Dułak, M.; Friis, J.; Groves, M. N.; Hammer, B.; Hargus, C. et al. The atomic simulation environment-a Python library for working with atoms. *J. Phys.: Condens. Matter* **2017**, *29*, 273002.
[51] Ke, Q.; Gong, X. T.; Liao, S. W.; Duan, C. X.; Li, L. B. Effects of thermostats/barostats on physical properties of liquids by molecular dynamics simulations. *J. Mol. Liq.* **2022**, *365*, 120116.

[52] Nosé, S. A unified formulation of the constant temperature molecular dynamics methods. *J. Chem. Phys.* **1984**, *81*, 511–519.
[53] Hoover, W. G. Canonical dynamics: Equilibrium phase-space distributions. *Phys. Rev. A* **1985**, *31*, 1695–1697.
[54] Kresse, G.; Joubert, D. From ultrasoft pseudopotentials to the projector augmented-wave method. *Phys. Rev. B* **1999**, *59*, 1758–1775.
[55] Kresse, G.; Furthmüller, J. Efficient iterative schemes for *ab initio* total-energy calculations using a plane-wave basis set. *Phys. Rev. B* **1996**, *54*, 11169–11186.
[56] Perdew, J. P.; Burke, K.; Ernzerhof, M. Generalized gradient approximation made simple. *Phys. Rev. Lett.* **1996**, *77*, 3865–3868.
[57] Grimme, S.; Antony, J.; Ehrlich, S.; Krieg, H. A consistent and accurate *ab initio* parametrization of density functional dispersion correction (DFT-D) for the 94 elements H–Pu. *J. Chem. Phys.* **2010**, *132*, 154104.
[58] Grimme, S.; Ehrlich, S.; Goerigk, L. Effect of the damping function in dispersion corrected density functional theory. *J. Comput. Chem.* **2011**, *32*, 1456–1465.
[59] Weng, T. T.; Schmidt, J. R. Flexible and transferable *ab initio* force field for zeolitic imidazolate frameworks: ZIF-FF. *J. Phys. Chem. A* **2019**, *123*, 3000–3012.
[60] Martin, M. G.; Siepmann, J. I. Transferable potentials for phase equilibria. 1. United-atom description of n-alkanes. *J. Phys. Chem. B* **1998**, *102*, 2569–2577.
[61] Batatia, I.; Benner, P.; Chiang, Y.; Elena, A. M.; Kovács, D. P.; Riebesell, J.; Advincula, X. R.; Asta, M.; Avaylon, M.; Baldwin, W. J. et al. A foundation model for atomistic materials chemistry. *J. Chem. Phys.* **2025**, *163*, 184110.
[62] Xu, J. B.; Liang, T.; Xu, K.; Lindgren, E.; Chen, Z. R.; Zhao, R.; Liu, J. H.; Berger, E.; Tang, B. R.; Zhang, B. H. et al. NEP89: Universal neuroevolution potential for inorganic and organic materials across 89 elements. 2025.
[63] Takamoto, S.; Shinagawa, C.; Motoki, D.; Nakago, K.; Li, W. W.; Kurata, I.; Watanabe, T.; Yayama, Y.; Iriguchi, H.; Asano, Y. et al. Towards universal neural network potential for material discovery applicable to arbitrary combination of 45 elements. *Nat. Commun.* **2022**, *13*, 2991.
[64] Gowers, R. J.; Linke, M.; Barnoud, J.; Reddy, T. J. E.; Melo, M. N.; Seyler, S. L.; Domański, J.; Dotson, D. L.; Buchoux, S.; Kenney, I. M. et al. MDAnalysis: A python package for the rapid analysis of molecular dynamics simulations. *SciPy*, DOI: 10.25080/Majora-629e541a-00e.
[65] Michaud-Agrawal, N.; Denning, E. J.; Woolf, T. B.; Beckstein, O. MDAnalysis: A toolkit for the analysis of molecular dynamics simulations. *J. Comput. Chem.* **2011**, *32*, 2319–2327.
[66] Stukowski, A. Visualization and analysis of atomistic simulation data with OVITO-the open visualization tool. *Model. Simul. Mater. Sci. Eng.* **2010**, *18*, 015012.
[67] Frenkel, D.; Smit, B. *Understanding Molecular Simulation: From Algorithms to Applications*; 3rd ed. Elsevier: San Diego, 2023.
[68] Widom, B. Some topics in the theory of fluids. *J. Chem. Phys.* **1963**, *39*, 2808–2812.
[69] Lindgren, E.; Rahm, M.; Fransson, E.; Eriksson, F.; Österbacka, N.; Fan, Z. Y.; Erhart, P. Calorine: A Python package for constructing and sampling neuroevolution potential models. *J. Open Source Softw.* **2024**, *9*, 6264.
[70] Tanaka, H.; Ohsaki, S.; Hiraide, S.; Yamamoto, D.; Watanabe, S.; Miyahara, M. T. Adsorption-induced structural transition of ZIF-8: A combined experimental and simulation study. *J. Phys. Chem. C* **2014**, *118*, 8445–8454.
[71] Hertäg, L.; Bux, H.; Caro, J.; Chmelik, C.; Remsungnen, T.; Knauth, M.; Fritzsche, S. Diffusion of CH_4 and H_2 in ZIF-8. *J. Membr. Sci.* **2011**, *377*, 36–41.
[72] Chakraborty, A.; Saha, B. B.; Ng, K. C.; Koyama, S.; Srinivasan, K. Theoretical insight of physical adsorption for a single component adsorbent + adsorbate system: II. *The henry region. Langmuir* **2009**, *25*, 7359–7367.
[73] Do, D. D.; Nicholson, D.; Do, H. D. On the Henry constant and isosteric heat at zero loading in gas phase adsorption. *J. Colloid Interface Sci.* **2008**, *324*, 15–24.
[74] Yampolskii, Y.; Pinnau, I.; Freeman, B. D. *Materials Science of Membranes for Gas and Vapor Separation*; John Wiley & Sons, Ltd: Chichester, 2006.
[75] Zhang, C.; Lively, R. P.; Zhang, K.; Johnson, J. R.; Karvan, O.; Koros, W. J. Unexpected molecular sieving properties of zeolitic imidazolate framework-8. *J. Phys. Chem. Lett.* **2012**, *3*, 2130–2134.
[76] Riebesell, J.; Goodall, R. E. A.; Benner, P.; Chiang, Y.; Deng, B. W.; Ceder, G.; Asta, M.; Lee, A. A.; Jain, A.; Persson, K. A. A framework to evaluate machine learning crystal stability predictions. *Nat. Mach. Intell.* **2025**, *7*, 836–847.
[77] Ying, P. H.; Fan, Z. Y. Combining the D3 dispersion correction with the neuroevolution machine-learned potential. *J. Phys.: Condens. Matter* **2024**, *36*, 125901.